Geophysical Journal International

Geophys. J. Int. (2013) **195,** 932–944
Advance Access publication 2013 August 2

doi: 10.1093/gji/ggt275

3-D characterization of high-permeability zones in a gravel aquifer using 2-D crosshole GPR full-waveform inversion and waveguide detection

Anja Klotzsche,[1] Jan van der Kruk,[1] Niklas Linde,[2] Joseph Doetsch[3] and Harry Vereecken[1]

[1] *Agrosphere (IBG-3), Forschungszentrum Jülich, Germany. E-mail: a.klotzsche@fz-juelich.de*
[2] *Applied and Environmental Geophysics Group, Faculty of Geosciences and the Environment, University of Lausanne, Switzerland*
[3] *Department of Geoscience, Aarhus University, Aarhus, Denmark*

Accepted 2013 July 9. Received 2013 July 8; in original form 2012 December 18

SUMMARY

Reliable high-resolution 3-D characterization of aquifers helps to improve our understanding of flow and transport processes when small-scale structures have a strong influence. Crosshole ground penetrating radar (GPR) is a powerful tool for characterizing aquifers due to the method's high-resolution and sensitivity to porosity and soil water content. Recently, a novel GPR full-waveform inversion algorithm was introduced, which is here applied and used for 3-D characterization by inverting six crosshole GPR cross-sections collected between four wells arranged in a square configuration close to the Thur River in Switzerland. The inversion results in the saturated part of this gravel aquifer reveals a significant improvement in resolution for the dielectric permittivity and electrical conductivity images compared to ray-based methods. Consistent structures where acquisition planes intersect indicate the robustness of the inversion process. A decimetre-scale layer with high dielectric permittivity was revealed at a depth of 5–6 m in all six cross-sections analysed here, and a less prominent zone with high dielectric permittivity was found at a depth of 7.5–9 m. These high-permittivity layers act as low-velocity waveguides and they are interpreted as high-porosity layers and possible zones of preferential flow. Porosity estimates from the permittivity models agree well with estimates from Neutron–Neutron logging data at the intersecting diagonal planes. Moreover, estimates of hydraulic permeability based on flowmeter logs confirm the presence of zones of preferential flow in these depth intervals. A detailed analysis of the measured data for transmitters located within the waveguides, revealed increased trace energy due to late-arrival elongated wave trains, which were observed for receiver positions straddling this zone. For the same receiver positions within the waveguide, a distinct minimum in the trace energy was visible when the transmitter was located outside the waveguide. A novel amplitude analysis was proposed to explore these maxima and minima of the trace energy. Laterally continuous low-velocity waveguides and their boundaries were identified in the measured data alone. In contrast to the full-waveform inversion, this method follows a simple workflow and needs no detailed and time consuming processing or inversion of the data. Comparison with the full-waveform inversion results confirmed the presence of the waveguides illustrating that full-waveform inversion return reliable results at the highest resolution currently possible at these scales. We envision that full-waveform inversion of GPR data will play an important role in a wide range of geological, hydrological, glacial and periglacial studies in the critical zone.

Key words: Downhole methods; Tomography; Ground penetrating radar; Hydrogeophysics; Guided waves; Wave propagation.

INTRODUCTION

A detailed characterization of aquifers may improve the prediction of flow in complex multiphase systems, such as the vadose zone, and the prediction of transport processes needed to evaluate contaminant hazards and clean-up potentials of contaminated aquifers (Hubbard *et al.* 2001; Binley *et al.* 2002a,b; Kemna *et al.* 2002). Traditional methods either have a small spatial sampling volume and a high resolution, such as logging tools or lab measurements of cores, or they capture an average response over a large

volume, such as pumping or tracer tests. Geophysical methods like ground penetrating radar (GPR), electrical resistivity tomography (ERT) and seismics can close the gap between these scales (Rubin *et al.* 1992; Hubbard & Rubin 2000; Binley *et al.* 2001; Garambois *et al.* 2002; Linde *et al.* 2006; Doetsch *et al.* 2010a; Slater *et al.* 2010; Cordua *et al.* 2012).

Detailed geophysical investigations at several test sites have improved our understanding of how different geophysical methods can be used to comprehend aquifer properties. Examples include the Boise Hydrogeophysical Research Site (BHRS) in the United States (Bradford *et al.* 2009; Dafflon *et al.* 2011), the Widen test site in Switzerland (Diem *et al.* 2010; Doetsch *et al.* 2010b; Coscia *et al.* 2012; Lochbühler *et al.* 2013) and the MADE site in the United States (Dogan *et al.* 2011; Zheng *et al.* 2011). These investigations have shown that GPR, ERT and seismics can provide porosity estimates for aquifers, and that each of these methods has different benefits and limitations. For example, porosity estimates based on seismic velocity are not as well constrained as those derived from radar wave velocity. For borehole deployments, the resolution of inferred seismic and radar parameters depends on the ray coverage of the measurements, which is typically high in the centre and low at the top and bottom of the acquisition plane. ERT images in contrast are better constrained close to the electrodes and less constrained between the boreholes (Day-Lewis *et al.* 2005).

In comparison with ERT and seismics, GPR returns images with the highest resolution for aquifers (Doetsch *et al.* 2010a), and several non-invasive surface and minimally invasive crosshole GPR measurements have been used to characterize the saturated aquifer and the vadose zone (Hubbard *et al.* 1997, 2001; Tronicke *et al.* 1999, 2002; Binley *et al.* 2001; Winship *et al.* 2006; Looms *et al.* 2008; Dorn *et al.* 2012). Another major advantage of GPR is that it can provide both relative dielectric permittivity ε_r and electrical conductivity σ. In low-loss conditions, the electromagnetic (EM) wave velocity at radar frequencies mainly depends on the relative dielectric permittivity ε_r of the medium. Due to the large contrast in dielectric permittivity between air ($\varepsilon_r \approx 1$) and distilled water ($\varepsilon_r \approx 80$ at 20 °C), this parameter can be used to determine the water content of the medium. The attenuation of the EM wave depends on the electrical conductivity σ of the medium, which is not only sensitive to the water content, but can also indicate clay content or pore-water salinity (Davis & Annan 1989; Tronicke *et al.* 2004).

Inversion algorithms are generally needed to estimate the subsurface distribution of physical properties. Suboptimal resolution is obtained by common ray-based seismic and GPR inversion algorithms that use first-arrival times or first-cycle amplitudes (Musil *et al.* 2006), or Fresnel volume radar-propagation velocity tomography (Buursink *et al.* 2008). These methods only account for a small fraction of the information contained in the data and typically use regularization in the form of damping or smoothing constraints to make the inversion algorithm robust and assure convergence to a unique solution.

In contrast, full-waveform inversion incorporates a significant part of the entire waveform in the inversion, including secondary scattered events, applies only smoothing of the updating gradients and does not require any damping parameters. The resulting spatial resolution of the ray-based methods depends on the diameter of the first Fresnel zone (Williamson 1991), whereas the full-waveform inversion can deliver results with subwavelength resolution (Wu & Toksoz 1987; Pratt & Shipp 1999). Since the pioneering work of Tarantola (1984), many research groups have further developed the full-waveform inversion approach and applied it to seismic data (Tarantola 1984, 2005; Shin & Cha 2008; Virieux & Operto 2009). In comparison with surface measurements, results from crosshole setups are better constrained due to the direct wave between the boreholes, the known borehole separation and the good ground coupling of the transmitters and receivers (Rao *et al.* 2006; Belina *et al.* 2009; Fichtner & Trampert 2011; Zhang *et al.* 2012).

Recently developed crosshole GPR full-waveform inversion was applied to synthetic (Ernst *et al.* 2007b; Kuroda *et al.* 2007) and experimental data (Ernst *et al.* 2007a; Belina *et al.* 2012). Ernst *et al.* (2007a,b) developed and applied a 2-D finite-difference time-domain (FDTD) code for crosshole GPR data, and Meles *et al.* (2010) incorporated the vectorial behaviour of the EM field and implemented a simultaneous update for permittivity and conductivity. Klotzsche *et al.* (2010) applied this algorithm to GPR data acquired in a gravel aquifer in Switzerland. After improving the starting models, an EM waveguide between the boreholes was imaged, which acted as a possible preferential flow path (Klotzsche *et al.* 2012). Such thin preferential flow paths (of higher porosity) or clay lenses play an important role for hydrological processes in aquifers (al Hagrey & Michaelson 1999; Day-Lewis *et al.* 2003; Ronayne & Gorelick 2006; Bianchi *et al.* 2011), but their restricted thickness often prevents standard methods (e.g. ray-based inversion) from detecting their exact position.

Increases in the water and clay content (high electrical conductivity) affect EM waves due to their reduced velocity. When the thickness of these layers is similar to the wavelength of the GPR signal, these layers act as low-velocity waveguides (Arcone 1984; Arcone *et al.* 2003; van der Kruk *et al.* 2009, 2010; Klotzsche *et al.* 2012; Strobach *et al.* 2013). Due to the reduced EM wave speed in these layers (increase in ε_r up to 25), total reflection of the wave occurs at the layer boundaries beyond the critical angle and causes multiple internal reflections of the wave. These multiple reflections form late-arrival and high-amplitude elongated wave trains, which can be captured in the measured signal. Late-arrival events, such as those caused by a waveguide, are ignored by ray-based methods and cannot be resolved. In contrast, the full-waveform inversion can resolve such layers because it incorporates all of these events.

In this paper, we determine the lateral extent of low-velocity waveguides using a pseudo-3-D full-waveform inversion of six crosshole GPR cross-sections within a square configuration of four boreholes. For each cross-section, we use a 2-D full-waveform inversion, and the inversion results are visualized in 3-D to characterize the aquifer geometry and the extensions of the low-velocity waveguides. A novel amplitude analysis is introduced to delimit wave-guiding structures by exploring the maxima and minima positions of the trace energy distributions of the measured data, which indicate the existence of wave-guiding structures. Using these positions, we are able to detect fast and efficient continuous waveguides and their boundaries without applying any inversion or detailed processing (necessary for full-waveform inversion). Finally, we compare the full-waveform inversion results with porosities inferred from Neutron–Neutron data and permeability logs based on EM flowmeter data acquired in the same boreholes, and show that the low-velocity waveguides are zones of high porosity and high permeability.

FULL-WAVEFORM INVERSION: THEORY

Important pre-processing steps for full-waveform inversion include the estimation of appropriate permittivity and conductivity starting models, and an effective source wavelet. The ε_r and σ starting models are obtained using first-arrival time and first-cycle

amplitude inversion. These starting models need to return synthetic data pulses that are offset less than one-half wavelength ($\lambda/2$) from the measured traces, otherwise the inversion can be trapped within a local minimum of the misfit function (Meles *et al.* 2011). This condition is verified during the source wavelet estimation, when synthetic data are calculated for the starting model. Additional constraints on the starting model are usually required close to the water table as it provides reflected waves caused by the high-permittivity contrast to the overlying unsaturated zone (Klotzsche *et al.* 2012). To apply the 2-D code to real data, 3-D propagation must be accounted for within the data. Following the approach of Ernst *et al.* (2007a), a 3- to 2-D transformation by Bleistein (1986) is performed based on the first-arrival time. Using the initial ε_r and σ tomograms obtained from the ray-based inversion, an initial source wavelet is obtained by averaging the normalized horizontally travelling pulses from each transmitter. At this point, only the shape of the source wavelet is considered, and no amplitude information is used. The amplitude and shape of the effective wavelet are corrected in a second step by applying a deconvolution approach (Ernst *et al.* 2007a; Klotzsche *et al.* 2010).

The full-waveform inversion is performed using the estimated effective source wavelet and the starting model. It is based on a conjugate gradient method that iteratively minimizes the misfit function C between the measured and modelled data such that $C = 0.5 \times \|\mathbf{E}^{\mathrm{mod}} - \mathbf{E}^{\mathrm{meas}}\|^2$, where $\mathbf{E}^{\mathrm{mod}}$ and $\mathbf{E}^{\mathrm{meas}}$ are vectors that contain modelled and measured traces, respectively, for all the transmitter–receiver combinations within a pre-defined time window. First, synthetic data are calculated with the 2-D FDTD code using the initial model parameters. The modelled wavefield is then used to calculate the residual wavefield by subtracting the measured data from the modelled data. By backpropagation of this residual wavefield through the model domain and cross-correlation with the modelled data, the ε_r and σ model gradients are calculated. These gradients of the data misfit function define the updating directions that are expected to reduce the misfit function. For the simultaneous updating of the ε_r and σ models, step lengths are computed using appropriate perturbation factors. Mathematical details of the calculation of the misfit function, gradient and step lengths are described in Meles *et al.* (2010). When the change in the misfit function C between two subsequent iterations is less than 1 per cent, the iterative approach is terminated, and the last iteration is considered as the final result. As the computational cost is high and memory requirements are too demanding for 3-D inversion, we construct pseudo-3-D models by stitching the 2-D inversion models together.

THUR RIVER TEST SITE AND DATA ACQUISITION

The test site is located in northeastern Switzerland close to the Thur River. Previous studies (Cirpka *et al.* 2007; Diem *et al.* 2010; Doetsch *et al.* 2010a,b; Klotzsche *et al.* 2010, 2012; Coscia *et al.* 2011, 2012; Lochbühler *et al.* 2013) indicated an aquifer comprising a 7-m-thick highly permeable glaciofluvial gravel deposit, embedded between overlying alluvial loam, with a thickness of 3 m and underlying low-permeable lacustrine sediments at a depth 10 m. The test site (Fig. 1a) consists of 18 boreholes that were slotted over the thickness of the aquifer. Coscia *et al.* (2012) indicated zones of preferential flow in the shallow-to-intermediate zone of the aquifer using ERT time-lapse experiments.

Using four boreholes arranged in a square, (see black circles in Figs 1a and b), a zonation based on joint inversion of crosshole GPR,

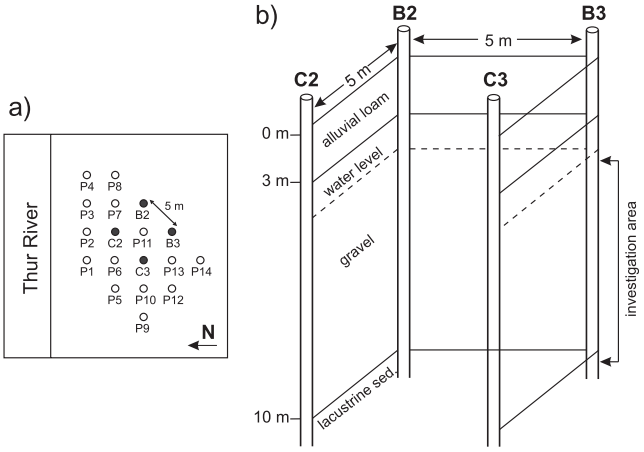

Figure 1. (a) Overview of the Widen test site with the borehole locations [modified from Coscia *et al.* (2012)]. The four black boreholes were used for the full-waveform inversion. (b) Schematic setup of the four boreholes used for the full-waveform inversion within the geological sequence. The aquifer comprised a 7-m-thick gravel layer embedded between alluvial loam in the top 3 m and underlying low permeable lacustrine sediments. The groundwater table was at a depth of approximately 4.2 m.

seismics and ERT data was performed revealing that the aquifer can be divided into three main lithological zones, where the middle layer is characterized by a significantly lower porosity (Doetsch *et al.* 2010a). Klotzsche *et al.* (2012) studied the acquisition plane between B3 and C3 using GPR full-waveform inversion and imaged a low-velocity waveguide at a depth of 5.3–6.1 m, which was not imaged using other geophysical techniques. Here, we characterized the waveguide zone at a depth of 5–6 m in three dimensions, and performed tomographic crosshole experiments using all six possible borehole combinations between the four boreholes followed by a comparison with independent geophysical logging data.

The GPR measurements were acquired using fibre optic cables and RAMAC 250 MHz dipole antennas, except for the cross-section B3–C2, where 100 MHz antennas were employed due to battery problems. We chose the same depth notation as Doetsch *et al.* (2010a,b), with the zero level being the top of the casing of borehole C2. For the measurements, we applied a semi-reciprocal setup by using a low number of transmitter positions with a spacing of 0.5 m, and a dense 0.1 m spatial sampling for the receiver positions below the groundwater table (at a depth of approximately 4.2 m). This approach reduces computational costs and acquisition time. To compensate for the reduced ray coverage close to the transmitter borehole, the transmitter and receiver boreholes were interchanged, and the measurements were repeated to improve the ray coverage close to the receiver well and to ensure an overall dense ray coverage (Klotzsche *et al.* 2010; Oberröhrmann *et al.* 2013). About 9–11 transmitters and 55–60 receivers were used for both semi-reciprocal measurements in every plane. Oberröhrmann *et al.* (2013) applied a resolution analysis to full-waveform inversion results for different transmitter–receiver configurations, and showed that the employed setup provides a good compromise between resolution and computational costs compared to other tested configurations.

FULL-WAVEFORM INVERSION RESULTS OF THE THUR RIVER AQUIFER

First, the crosshole GPR data were pre-processed by applying a time-zero correction and a bandpass filter to remove the noise outside

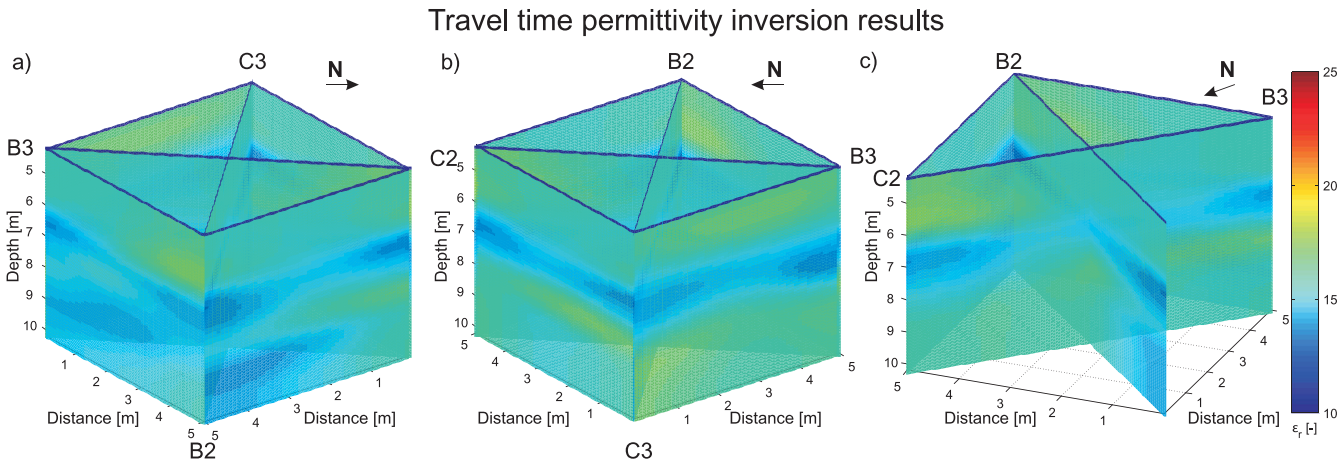

Figure 2. Relative permittivity results of the traveltime inversion for different viewing angles. See Fig. 1 for the borehole notation. These results serve as starting models for the full-waveform inversion. The vadose zone was included with a lower permittivity above a depth of 4.2 m.

the source spectrum. Secondly, ray-based inversions using curved rays were applied to obtain starting models. The first-arrival traveltime inversion results based on the data of Doetsch *et al.* (2010a) were used as ε_r starting models, as shown in Fig. 2. The ray-based tomographic inversion models were a smooth representation of the stratigraphy, and generally three zones were observed with a low ε_r layer embedded between two intermediate ε_r layers. To account for the strong contrast between the unsaturated and saturated zones, which was not resolved by the traveltime inversion, the vadose zone above 4.2 m was attributed a relative permittivity of $\varepsilon_r = 5$, and a homogenous layer was introduced at a depth of 4.2–5.5 m with $\varepsilon_r = 17$. For these values, the first-arrival times of the modelled and measured data showed an overlap of at least half a wavelength. For σ, we used a homogeneous starting model with 9.5 mS m^{-1}, representing the mean of the first-cycle amplitude inversion results.

Using the obtained starting models for each of the six cross-sections, an initial source wavelet for each cross-section was estimated by averaging the normalized horizontally travelling pulses from each transmitter. Next, effective wavelets were calculated by applying the deconvolution approach (Figs 3a and b). A similar shape and amplitude of the wavelet was observed for all cross-sections where the 250 MHz antennas were used, whereas the diagonal plane C3–B2 had slightly higher amplitudes. In Fig. 3(c), the normalized amplitude profiles for each of the six cross-sections are plotted. The centre frequencies and frequency bandwidth for all cross-sections with the 250 MHz antennas were very similar, as expected from the results presented in Fig. 3(a). Note, that the effective centre frequency is significantly lower than the nominal centre frequency, due to the fact that the antennas are electrically longer in high-permittivity media and emit lower frequencies than when they are placed in air. Similar wavelets were observed for all angles, which indicates that our numerical approach to model the antennas as infinitesimal dipoles is suitable. In the modelling, the dipole antennas were present at the position of the feed gap of the true antennas. When transmitter–receiver combinations are used with larger angles, differences in the wavelets might occur, and the finite length of the antennas must be included. Antennas with finite length can be implemented in the FDTD code using the approach of Arcone (1995) and Streich & van der Kruk (2007).

The full-waveform inversion results for ε_r (Fig. 4) show higher resolution images than the traveltime inversion results (Fig. 2). The high ε_r zone at a depth of 5–6 m for plane B3–C3, which was inferred by Klotzsche *et al.* (2012), can be identified in all other cross-sections. Another high ε_r layer was observed at a depth of 7.5–9 m, for example, in planes C2–C3 and C3–B3. We obtained similar results for all of the 2-D tomograms at the borehole locations, and at the intersection of the diagonals. Only the upper parts of the diagonal sections show less similarity at the intersection.

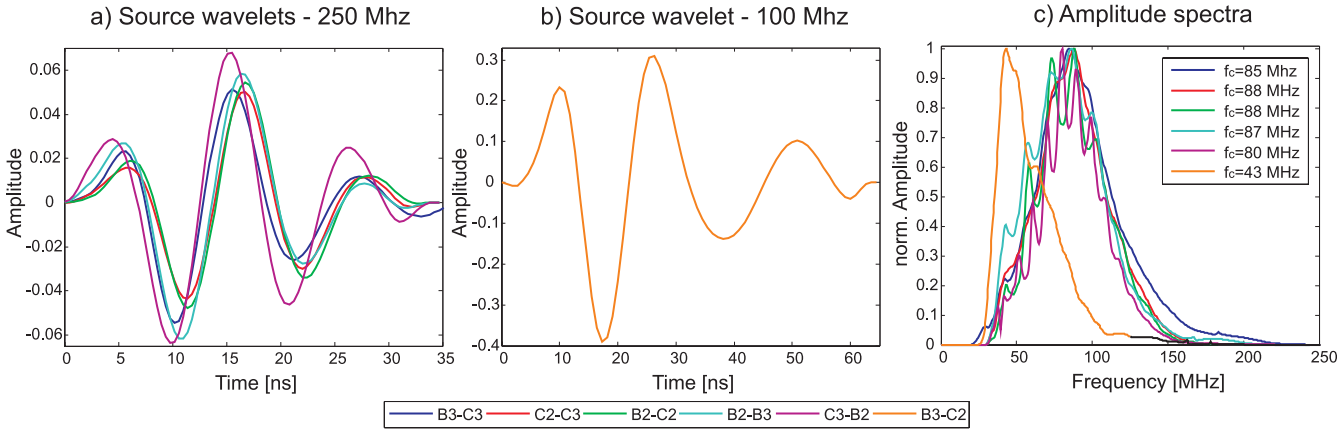

Figure 3. (a and b) The estimated effective source wavelets for the cross-sections where the 250 MHz antenna or the 100 MHz antenna were used, respectively. Each colour in this figure represents a different plane. In (c), the corresponding normalized amplitude profiles are shown for the six different source wavelets. A similar shape, amplitude and centre frequency was obtained for the cross-sections measured with the 250 MHz antennas, shown in blue, red, green and cyan.

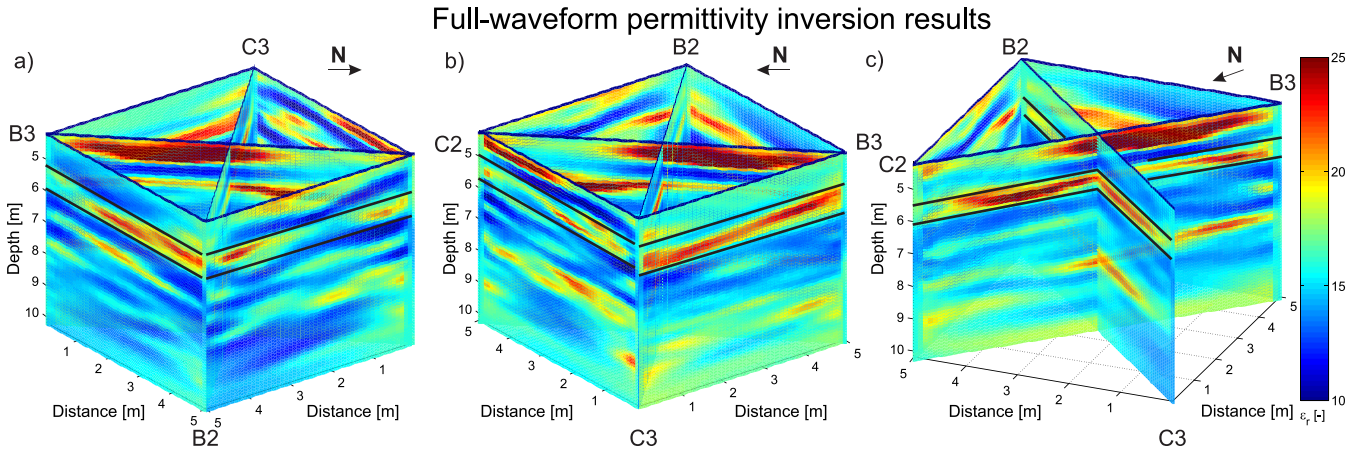

Figure 4. Permittivity results of the full-waveform inversion for different viewing angles. See Fig. 1 for the borehole notation. The black lines indicate the high-permittivity zone at a depth of 5–6 m.

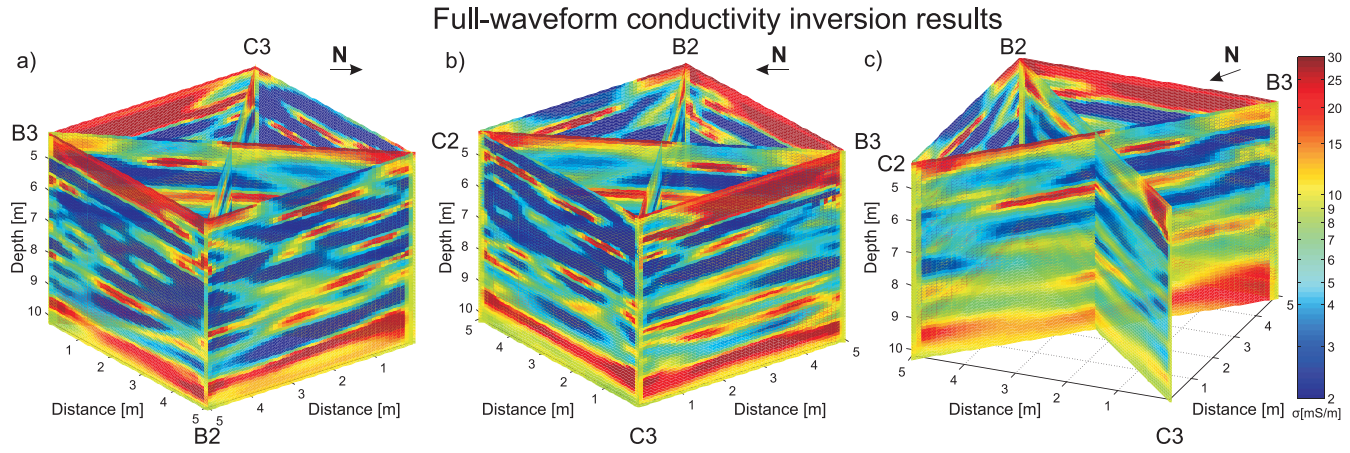

Figure 5. Conductivity results of the full-waveform inversion for different viewing angles. See Fig. 1 for the borehole notation.

The corresponding 3-D σ images from the full-waveform inversion show in all tomograms clearly the underlying lacustrine sediments (elevated clay content) indicated by high-conductivity values below a depth of 9.5 m (Fig. 5). These inversion results were achieved without *a priori* information. In contrast, 3-D ERT inversion required constraints on the actual boundaries to obtain models in agreement with the geological logs (Coscia *et al.* 2011). Although late-arrival amplitudes caused by the high ε_r zone are not correctly processed using the 3- to 2-D conversion, the intermediate conductivities obtained at a depth of 5–6 m indicate a change in the porosity rather than a change in the clay content as the cause of the increase in ε_r.

For all of the acquisition planes, a good agreement was obtained between the measured and full-waveform modelled data in terms of shape and amplitude of the waveforms, as shown in Figs 6(a)–(c) for plane B3–C3 (transmitter located in borehole C3). The ray-based modelled data (Fig. 6b) show only a good match of the first-arrival times, but the fit for later-arrivals times and amplitudes is less satisfactory. In contrast, the full-waveform inversion data (Fig. 6c) show an excellent fit of amplitude and phase, including small nuances in the radargrams, which indicates that the full-waveform inverted model well explains the measured data. Similar to previous experiences with field data (Ernst *et al.* 2007a; Klotzsche *et al.* 2010; Oberröhrmann *et al.* 2013), rms error between the measured and modelled data for each tomogram was reduced by at least 50 per cent compared to the ray-based inversion starting model.

To test the consistency between inversion results, we calculated correlation coefficients (R^2) at the intersections of cross-sections at borehole locations and the crossing of the diagonal planes at P11, for permittivity and conductivity (Table 1). For the calculation, we used the mean of two inversion cells next to the borehole. A high mean R^2 value of 0.88 was obtained for permittivity, whereas the mean R^2 value for conductivity was lower at 0.25 indicating that the conductivity values are less reliable. To improve the accuracy of conductive values more transmitter and receiver position could be used (Oberröhrmann *et al.* 2013) or a combined wavelet and conductivity updating could be implemented [similar to Busch *et al.* (2012)]. A total of 23 CPUs (for each transmitter and one master) were needed for the full-waveform inversion and an entire inversion took approximately 30 min using an MPI parallelized code on the JUROPA cluster at Forschungszentrum Jülich. Improved and more consistent conductivity results could possibly be obtained if cross-sections were inverted together, such that the estimated permittivities and conductivities at intersections are enforced as sometimes done in 2-D ray-based inversions (Musil *et al.* 2006; Dafflon *et al.* 2011).

WAVEGUIDE DETECTION THROUGH AMPLITUDE ANALYSIS

Similarly to Klotzsche *et al.* (2012) and Strobach *et al.* (2012), we consistently observe for transmitters located within waveguide

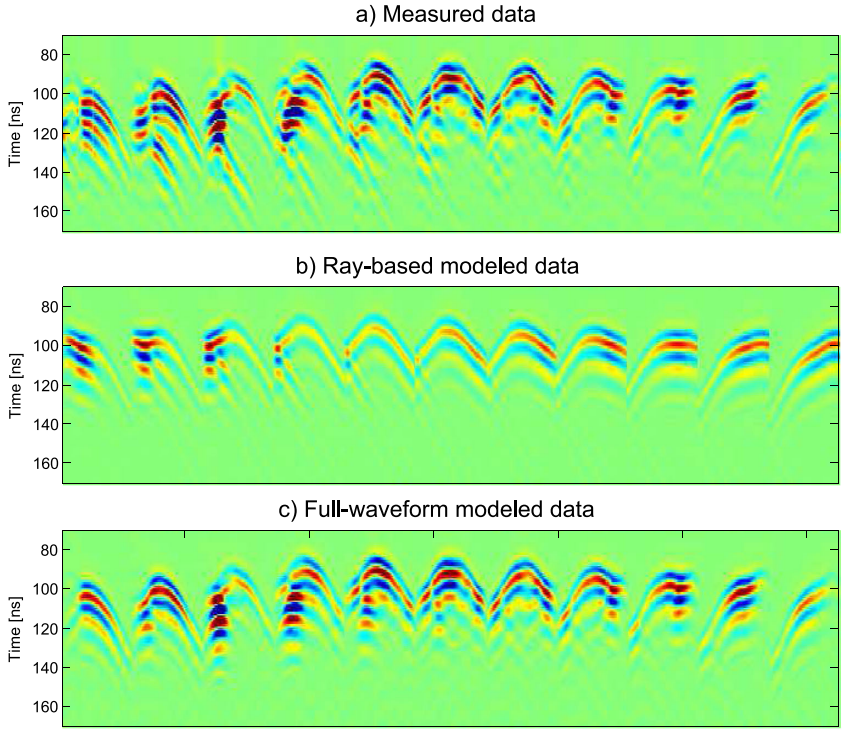

Figure 6. (a) Measured, (b) ray-based modelled and (c) full-waveform modelled data for section B3–C3 (transmitter in C3). The transmitter positions are indicated by T1 until T11, whereas T1 is located close to the water table and T11 at the bottom of the aquifer.

Table 1. Correlations coefficient R^2 for the full-waveform inversion permittivity and conductivity results at the four boreholes. The mean values of R^2 for the permittivity and conductivity planes were 0.88 and 0.26, respectively.

Borehole	B3			C3			C2			B2			P11
Planes	B3–C3 B2–C3	B3–C3 B3–C2	B2–B3 B3–C2	B3–C3 C3–C2	B3–C3 C3–B2	C3–C2 C3–B2	C3–C2 C2–B2	C3–C2 B3–C2	C2–B2 B3–C2	C2–B2 B2–B3	C2–B2 C3–B2	B2–B3 C3–B2	B2–C3 B3–C2
$R^2(\varepsilon)$	0.90	0.87	0.96	0.75	0.87	0.85	0.81	0.90	0.92	0.87	0.92	0.92	0.84
$R^2(\log(\sigma))$	0.17	0.32	0.29	0.16	0.42	0.18	0.21	0.19	0.53	0.29	0.18	0.09	0.24

zones late-arrival and high-amplitude elongated wave trains for receivers straddling the high-contrast layer. An example is transmitter T2 of cross-section B3–C3 (transmitter located in B3), where the wave trains are formed by internal multiple reflections beyond the critical angle, which interfere constructively to produce high-amplitude data and trap the energy within this low-velocity zone (see Fig. 7a). The corresponding modelled radargram for T2, as obtained from the final full-waveform inversion models, shows a good agreement for the guided wave arrivals (Figs 7a and b). The black lines indicate the position of the waveguide as detected by the full-waveform inversion. Similar high-amplitude elongated wave trains can be observed in the measured and modelled data for transmitter T3 in the cross-section B3–C3 (not shown).

Elongated wave trains, as observed in measured data of T3 (Fig. 7a), show a distinct maximum peak in the trace energy distribution (summation of the squared amplitude), and the energy for such traces is one to two orders of magnitude higher than the recorded trace outside the waveguide layer, as shown in Fig. 7(c) for the trace energy profiles of T2 and T3. For transmitters located outside the waveguide (e.g. Figs 7d and e) such as transmitter T7 of cross-section B3–C3, intermediate amplitudes were observed for most of the receivers. However, receivers positioned within the waveguide showed significantly diminished amplitudes. This behaviour is visible in the trace energy profile of transmitter T7 (Fig. 7f), exhibiting a clear minimum at a depth of 5.4 m around the previously found maxima positions (minima positions should be located close to the maxima positions). Similar behaviour was also observed in all other radargrams where transmitters were located outside the low-velocity waveguide (Fig. 7f). A possible explanation could be destructive interferences of the EM head waves from above and below the waveguide, which cause a minimum in the trace energy.

We also located high-amplitude elongated wave trains and diminished amplitudes for the other transmitter–receiver combinations, but concentrated on the dominant features linked to the high-permittivity zone at a depth of 5–6 m, which is present in all planes. Such clear maxima and minima positions of the trace energies as shown in Fig. 7 were not always observed. For example, for the cross-section C3–C2 and the transmitters located in C2, only one transmitter showed late-arrival elongated wave train events and the corresponding distinct maximum in the trace energy (see transmitter T14 in Figs 8a–c). Identifying the minima positions for the rest of the transmitters around the maximum position was also more challenging (as shown in Figs 8d–f). The less distinct minima positions were probably caused by the lateral heterogeneity within the high-permittivity structure (see also Fig. 4b). Further, clear maximum amplitudes were observed for transmitters at a depth between

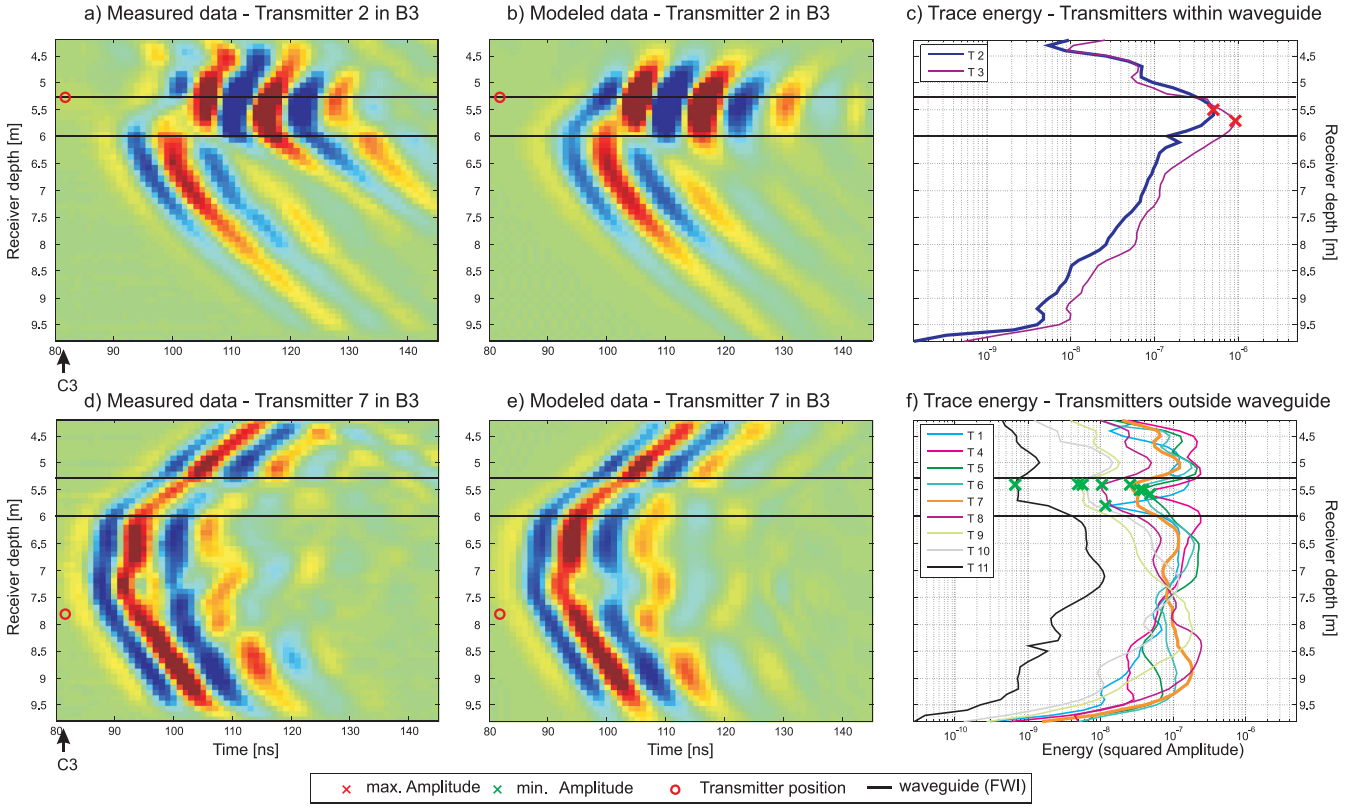

Figure 7. (a, b) Image plots of the measured and modelled data of transmitter 2 in cross-section B3–C3, respectively. Transmitter 2 is taken as an example of a transmitter located within the waveguide structure observed in Fig. 4. The red circle indicates the depth of the transmitter located in B3. (c) Corresponding trace energy profiles for all transmitters of the measured data located in the waveguide. The thick blue line indicates the profile corresponding to the image plot in (a). The red crosses indicate the position of the energy maximum. (d, e) Image plots of the measured and modelled data of transmitter 7, respectively. Transmitter 7 is taken as an example of a transmitter located outside the waveguide structure. (f) Corresponding trace energy profiles for all transmitters of the measured data located outside the waveguide. The thick orange graph indicates the profile corresponding to the image plot in (d). The green crosses indicate the position of the energy minimum within the waveguide.

7 and 8 m because of the high-permittivity range at these depths (see also Fig. 4b).

In the next step, the identified maxima and minima positions of the energy profiles of section B3-C2 are plotted against receiver depth and compared with the full-waveform inversion results close to borehole C3 (Figs 9a and b). It appears that the minima position for increasing depth converges with the upper waveguide boundary close to the borehole. Due to the restricted distance to the water table for the transmitter positions above the waveguide layer in the saturated aquifer, the minima indicating the lower waveguide boundary were not as definite here. For the second example of cross-section C3–C2, shown in Figs 9(c) and (d), the identification of the boundaries using the measured data was less straightforward, which was probably caused by the heterogeneity of the high-permittivity zone of the plane close to the borehole.

For the depth range between 7.5 and 9 m, additional distinct elongated wave trains (e.g. for plane C3-C2 in Fig. 8d) and corresponding minima positions were found, pertaining to high-permittivity structures present in the tomograms of C3–C2, C3–B2 and B3–C3 (see Fig. 4). Generally, a similar analysis could be carried out; however, choosing maxima and minima positions was more challenging for these zones, and they were not present in all cross-sections. Hence, the accuracy of boundary determination is influenced by the homogeneity of the waveguide.

We applied our approach of detecting maxima and minima positions to the data sets of all six cross-sections for the distinct waveguide at a depth of 5–6 m (Fig. 10). In some cases, it was more problematic to define a clear boundary from the minima trace energy picks (indicated with light green crosses). For example, for the transmitter located in C2 (Fig. 10b), it appears that two upper boundaries are possible to identify (indicated by dashed lines). The accuracy also decreases for the diagonals (see Figs 10e and f, right columns), and picking is more challenging, especially in the case of discontinuous layering of wave-guiding structures. The spatial transmitter position sampling of 0.5 m enabled a detailed detection of the waveguide effects. A sparser spatial sampling of transmitter and receiver would probably have reduced the ability to detect and identify the waveguide structures. The general view that permittivity dominates the traveltime and that conductivity dominates the amplitude of the signal must be revised, because the amplitudes are strongly influenced by the permittivity contrast in the presence of a waveguide.

PETROPHYSICAL INTERPRETATION AND COMPARISON WITH LOGGING DATA

We transformed the permittivity tomograms of each plane into porosities to characterize the aquifer and evaluate the waveform inversion results. We compared these porosities with Neutron–Neutron porosity and hydraulic permeability logs (Tchang 2012;

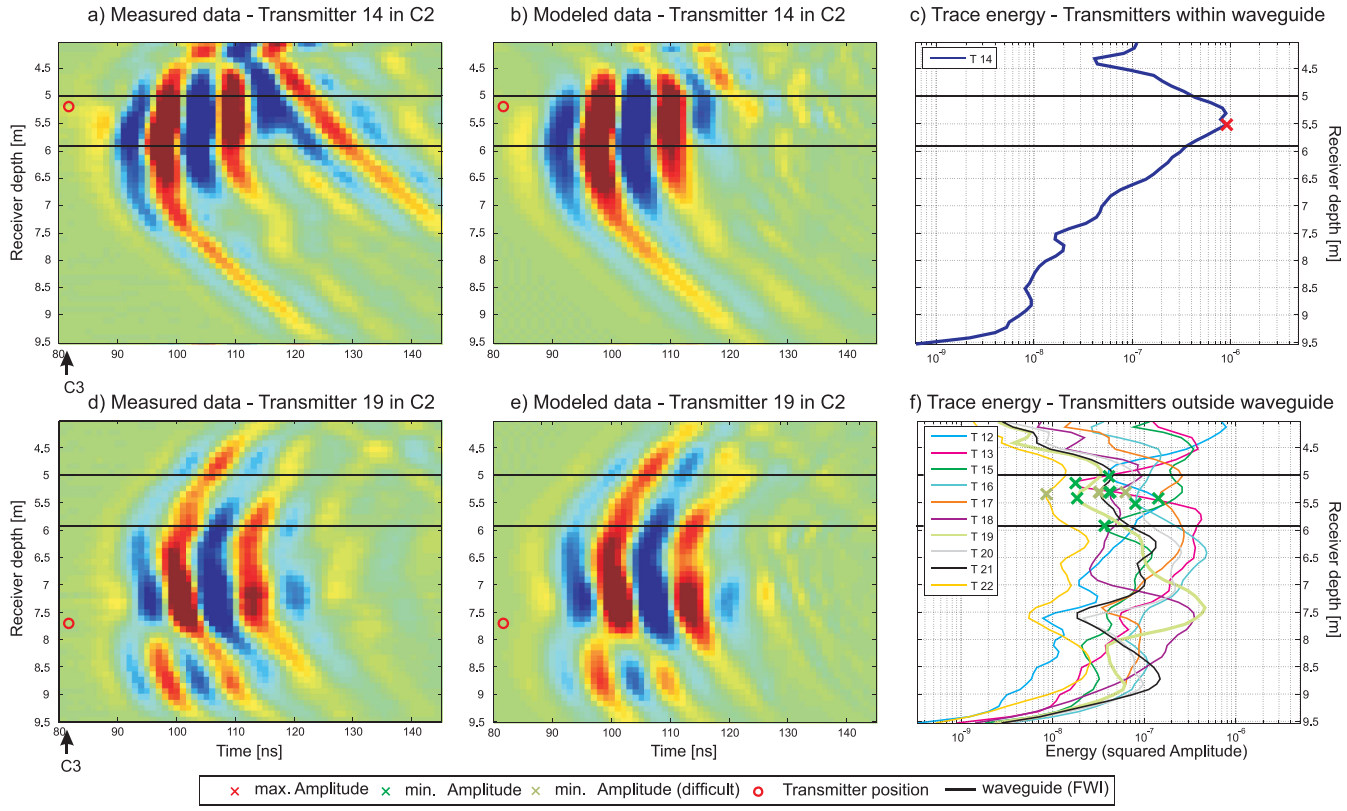

Figure 8. (a, b) Image plots of the measured and modelled data of transmitter 14 of cross-section C3–C2, respectively. Transmitter 14 is taken as an example of a transmitter located within the waveguide structure observed in Fig. 4. The red circle indicates the depth of the transmitter located in C3. (c) Corresponding trace energy profiles for all transmitters of the measured data located in the waveguide. The red crosses indicate the position of the energy maximum. (d, e) Image plots of the measured and modelled data of transmitter 19, respectively. Transmitter 19 is taken as an example of a transmitter located outside the waveguide structure. (f) Corresponding trace energy profiles for all transmitters of the measured data located outside the waveguide. The thick light green line indicates the profile corresponding to the image plot in (d). The green crosses indicated the position of the energy minimum within the waveguide.

Lochbühler *et al.* 2013). For the transformation of the permittivity, we followed the same approach as Pride (1994) and Doetsch *et al.* (2010a) using

$$\varepsilon = \frac{1}{F}\left[\varepsilon_{\mathrm{W}} + (F-1)\varepsilon_{\mathrm{S}}\right] = \frac{\varepsilon_{\mathrm{W}}}{F} + \varepsilon_{\mathrm{S}} - \frac{\varepsilon_{\mathrm{S}}}{F}, \tag{1}$$

$$F = \Phi^{-m} \tag{2}$$

and

$$\Phi = \sqrt[m]{\frac{\varepsilon - \varepsilon_{\mathrm{S}}}{\varepsilon_{\mathrm{W}} - \varepsilon_{\mathrm{S}}}}, \tag{3}$$

where F is the formation factor and Φ the porosity. Here, we used $\varepsilon_{\mathrm{W}} = 84$ as the relative permittivity of water (at 10 °C), $\varepsilon_{\mathrm{S}} = 8$ as the relative permittivity of the solid matrix, and the cementation factor was $m = 1.4$. A positive correlation exists between permittivity and converted porosity (compare Figs 4 and 11).

All waveguide boundaries identified using the amplitude analysis (see Fig. 10 and dark green boxes in Fig. 11) were confirmed, and in most cases, the boundaries obtained from the full-waveform inversion agreed well with the boundaries obtained by the energy analysis. The correspondence between the diagonal planes was less clear due to the increased distance and the reduced resolution caused by lower angular coverage and increased data errors. When the waveguide was discontinuously layered, the amplitude analysis approach was less accurate (see Figs 9c and d), whereas these heterogeneous structures were also resolved by the full-waveform inversion. In addition to the dominant waveguides between 5 and 6 m depth (dark green boxes in Fig. 11), we also indicate thinner waveguides present between 7 and 8 m depth that could be identified using at least one maxima and five minima (light green boxes in Fig. 11).

The permeability logs, normalized to the maximum of each log, were obtained using EM flowmeter data, in which the difference of the vertical flow in the boreholes was determined by subtracting the ambient flow from a flow measurement during a stable injection [see Tchang (2012) for details]. Within the hydraulic permeability logs, we observed a zone with higher permeability at a depth of 5–6 m, and an intermediate zone at a depth of 7.5–9 m. These zones were also found to have higher values in the porosity images obtained from the waveform inversion. Generally, for all the cross-sections, we obtained a good fit between the permeability logs and the high-porosity zones for the permittivity models of all planes. Furthermore, in the porosity images and in the permeability logs, we observed a decrease in the thickness of the high-porosity zone at 5–6 m towards the Thur River. This change in thickness is indicated by the tomogram C2–B2 (approximate thickness 0.3–0.4 m), which was located close to the Thur River in comparison to the tomogram B3–C3 (approximate thickness 0.6 m), which was furthest away from the river.

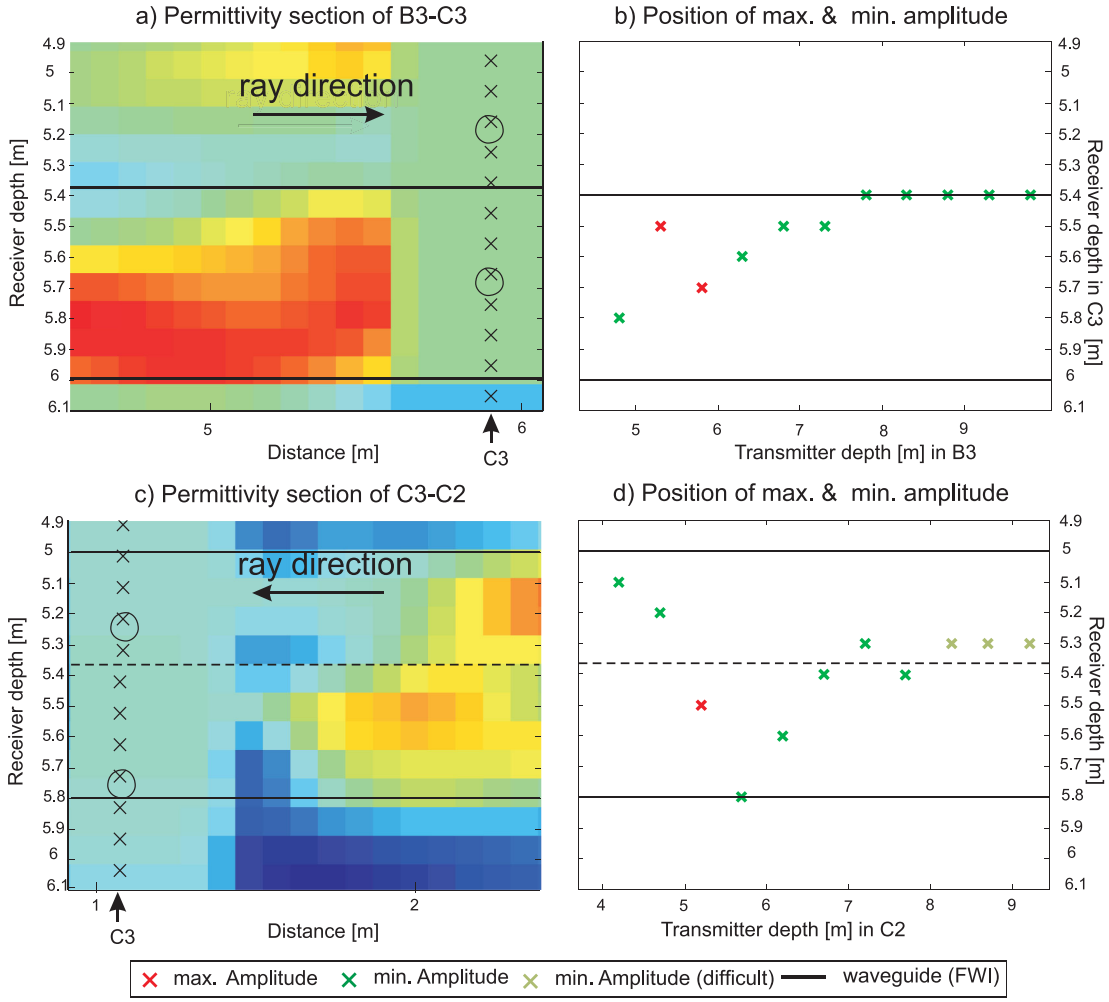

Figure 9. (a) Permittivity section of the waveguide in cross-section B3–C3 close to the borehole C3 (see Fig. 4). The black lines indicate the waveguide boundaries observed from the full-waveform inversion close to the corresponding borehole. The circles and crosses indicate the transmitter and receiver positions. For comparison, the maximum and minimum positions obtained in Figs 7(c) and (f) are plotted in (b) along the receiver depth, where the red and green crosses indicate the chosen maxima and minima position of the trace energy. (c) Permittivity section of the waveguide in plane C3–C2 close to the borehole C3 (see Fig. 4). For comparison, the maximum and minimum positions obtained in Figs 8(c) and (f) are plotted in (d) along the receiver depth.

For the diagonal planes, we performed a direct comparison at the intersection of the C3–B2 and B3–C2 sections, where Neutron–Neutron porosities were acquired in borehole P11 (see Fig. 1 for the location). Details of the calculations were given by Klotzsche *et al.* (2010). For each depth in the C3–B2 and B3–C2 planes, we computed the mean of three cells (each 9 cm) of the porosity models (see legend for corresponding colour) and compared these means with the measured porosity log (black graph) in Fig. 11(f). First of all, the porosity results of the full-waveform inversion between depths of 5 and 10 m were overall very similar, whereas some differences occurred in the upper metre. A comparison of the full-waveform porosities with the Neutron–Neutron porosity logs showed that they agreed well at a depth of 6–9.5 m. For the upper metre, the measured porosity was between the porosities obtained from the two permittivity tomograms.

To evaluate the full-waveform porosities, we calculated the correlation coefficient (R^2), the mean absolute error (MAE) and the rms error between the Neutron–Neutron porosities of P11 and the porosity graphs of the diagonal porosity planes (Fig. 11f) for the depth range of 6–9.5 m. For plane C3–B2, a higher correlation and smaller misfit with the porosity of P11 was obtained compared to the plane B3–C2 (Table 2). A possible explanation could be the difference in antenna frequency used for the GPR measurements. The lower frequency antenna used for the B3-C3 section results in larger wavelength and lower resolution.

CONCLUSIONS

We performed a 3-D characterization of a gravel aquifer using 2-D full-waveform inversion of six cross-sections in a set of four boreholes arranged in a square configuration. The independent decimetre-resolution full-waveform inverted cross-sections revealed good consistency in terms of permittivity at their intersection. In all conductivity images, the underlying lacustrine sediments were clearly observed without relying on any *a priori* information. However the consistency of the conductivity results is less satisfactory. A good fit was achieved for all tomograms between the measured and full-waveform modelled data in shape and amplitude, including the high-amplitude and late-time arrival events, which indicates reliability of the results. All models showed a high-permittivity layer at a depth of 5–6 m, and a second less extended layer with

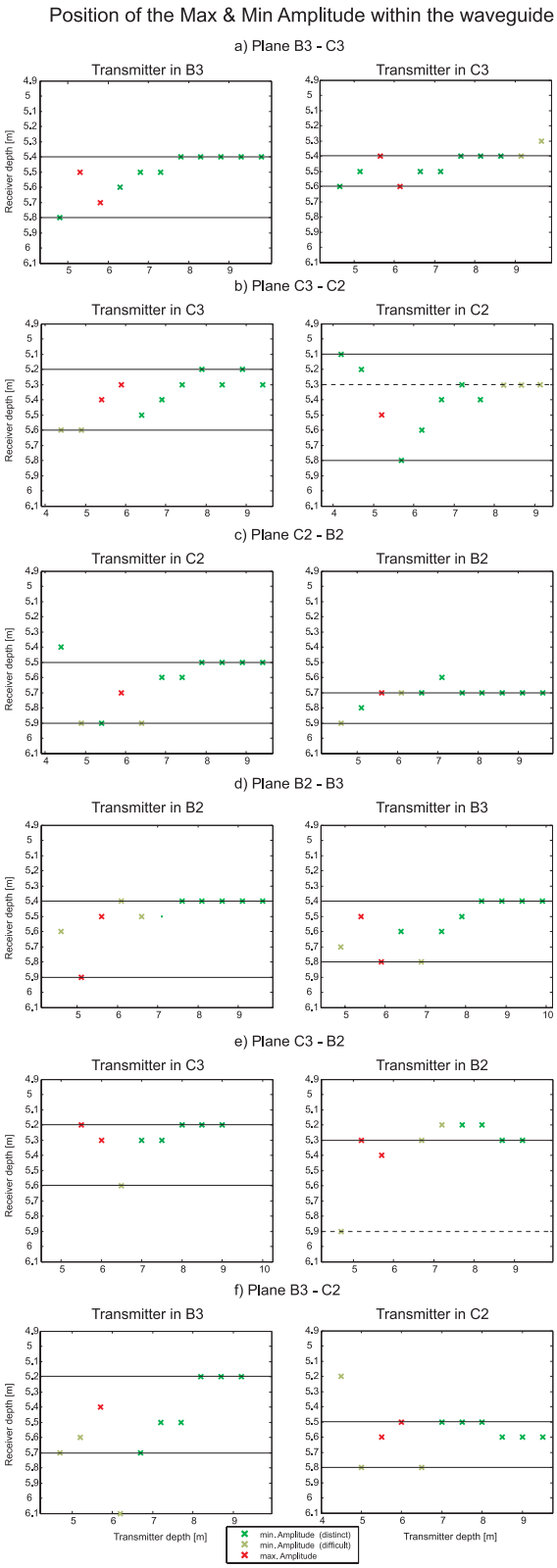

Figure 10. Position of the energy distribution maxima (red crosses) and minima (green crosses) for all cross-sections along the receiver depth. The dark green crosses indicate distinct minima position, whereas the light green crosses indicate difficult minima positions. The black lines indicate the estimated upper and lower boundaries of the waveguides obtained by the amplitude analysis using the maxima and minima positions of the trace energy profiles close to the corresponding borehole.

high-permittivity layer at a depth of 7.5–9 m. These high-permittivity zones acted as low-velocity waveguides for EM waves.

For transmitters located in the wave-guiding layer, high-amplitude and late-arrival elongated wave trains were present at receivers straddling the waveguide zone. In contrast, for transmitter positions outside the waveguide layer, diminished amplitudes were observed for receivers located within the waveguide. With increasing distance of the transmitter above and below the waveguide, these minima positions corresponded well with the lower and upper boundary of the full-waveform inverted continuous waveguides, respectively. This novel amplitude analysis was applied to the other measured crosshole data sets, and the obtained waveguide boundaries were confirmed by the full-waveform inversion results. For discontinuous waveguides, the results obtained were less clear. More research with synthetic studies is necessary to explore the potential and limitations of the amplitude analysis in more detail in the case of discontinuous, heterogeneous and dipping waveguides. Nevertheless, this new method is able to provide fast and efficient information about the position and dimension of waveguides without applying any inversion or advanced processing of the data. The full-waveform inversion can provide high-resolution images between the boreholes using several processing steps (e.g. starting models, source wavelet estimation) and more computational costs.

The obtained full-waveform inversion results were compared with porosity estimates from Neutron–Neutron and hydraulic permeability logs. While the logging data provide detailed information close to the wells, the full-waveform inversion returns a high-resolution porosity distribution between the boreholes. The peaks of the permeability and porosity logs agreed well with the high-permittivity waveguide layers of the full-waveform inversion at a depth of 5–6 m and 7.5–9 m, and the consistency of the results obtained and the data fit for all the cross-sections showed that full-waveform inversion returns reliable images with the highest resolution currently possible at these scales. The full-waveform inversion and the novel amplitude analysis can be applied as a minimally invasive method to characterize subwavelength structures for a wide range of applications, and it can improve our ability to image important small-scale structures in the critical zone.

More research is necessary to quantify the uncertainties of the waveform inversion models using different starting models, and synthetic modelling is required to understand the phenomena that cause the presence of a minimum in the trace energy. Further developments in full-waveform inversion should concentrate on the extension of the forward model to 3-D, and a combined 2-D inversion of more than one cross-section to get more consistent conductivity models at the borehole locations.

ACKNOWLEDGEMENTS

We thank the Jülich Supercomputing Center (JSC) for providing access to the JUROPA high-performance cluster. We also thank Tiffany Tchang for performing and providing the porosity and permeability logs from the Widen test site. Further, we thank the RECORD project, the Swiss National Science Foundation (SNF) and the ETH Competence Center for Environment and Sustainability (CCES) for funding and for making the data available for this study. JD was partially funded by DOE-LBNL under contract number DE-AC02-05CH11231. We thank Steve Arcone and Elmar Strobach for their detailed reviews that significantly improved the paper.

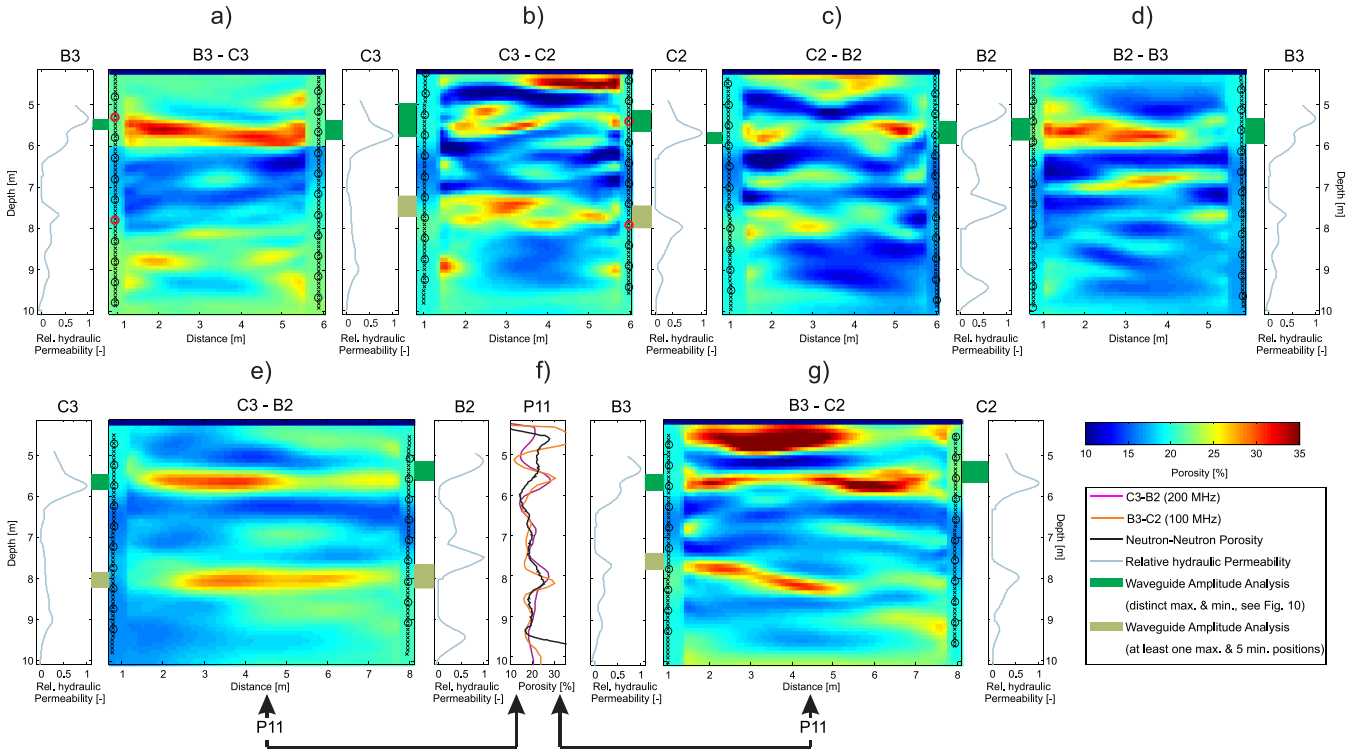

Figure 11. Converted porosities from the full-waveform inversion (images) in comparison to relative hydraulic permeabilities measured directly in the boreholes (graphs). Transmitter and receiver positions are indicated by circles and crosses, respectively. The transmitters coloured in red are used in Figs 7 and 8. (f) The Neutron–Neutron porosities of P11 are plotted with the corresponding response from the full-waveform inversion porosities close to the boreholes. The different colours of the graphs indicate the affiliations to the corresponding planes. The green box between the full-waveform inversion porosities and the permeability log indicate the thicknesses of the wave-guiding structures estimated using the amplitude analysis approach (see Fig. 10), where the dark green boxes indicate waveguides where all transmitter positions showed either a maximum or an minimum positions, and the light green boxes indicate waveguides with at least one maxima and five minima positions.

Table 2. Correlation coefficients (R^2), mean absolute errors (MAE) and rms errors between the porosities obtained from the full-waveform inversion for the diagonal planes and the Neutron–Neutron porosities of P11 at a depth of 6–9.5 m.

	R^2	MAE (%)	rms (%)
C3–B2	0.82	1.56	1.87
B3–C2	0.57	1.69	2.15

REFERENCES

al Hagrey, S.A. & Michaelson, J., 1999. Resistivity and percolation study of preferential flow in vadose zone at Bokhorst, Germany, *Geophysics,* **64,** 746–753.

Arcone, S.A., 1984. Field observations of electromagnetic pulse-propagtion in dielectric slabs, *Geophysics,* **49,** 1763–1773.

Arcone, S.A., 1995. Numerical-studies of the radiation-patterns of resistively loaded dipoles, *J. appl. Geophys.,* **33,** 39–52.

Arcone, S.A., Peapples, P.R. & Liu, L.B., 2003. Propagation of a ground-penetrating radar (GPR) pulse in a thin-surface waveguide, *Geophysics,* **68,** 1922–1933.

Belina, F.A., Ernst, J.R. & Holliger, K., 2009. Inversion of crosshole seismic data in heterogeneous environments: comparison of waveform and ray-based approaches, *J. appl. Geophys.,* **68,** 85–94.

Belina, F., Irving, J., Ernst, J. & Holliger, K., 2012. Evaluation of the reconstruction limits of a frequency-independent crosshole georadar waveform inversion scheme in the presence of dispersion, *J. appl. Geophys.,* **78,** 9–19.

Bianchi, M., Zheng, C.M., Wilson, C., Tick, G.R., Liu, G.S. & Gorelick, S.M., 2011. Spatial connectivity in a highly heterogeneous aquifer: from cores to preferential flow paths, *Water Resour. Res.,* **47,** doi:10.1029/2009wr008966.

Binley, A., Winship, P., Middleton, R., Pokar, M. & West, J., 2001. High-resolution characterization of vadose zone dynamics using cross-borehole radar, *Water Resour. Res.,* **37,** 2639–2652.

Binley, A., Cassiani, G., Middleton, R. & Winship, P., 2002a. Vadose zone flow model parameterisation using cross-borehole radar and resistivity imaging, *J. Hydrol.,* **267,** 147–159.

Binley, A., Winship, P., West, L.J., Pokar, M. & Middleton, R., 2002b. Seasonal variation of moisture content in unsaturated sandstone inferred from borehole radar and resistivity profiles, *J. Hydrol.,* **267,** 160–172.

Bleistein, N., 1986. 2–1/2 dimensional inplane wave-propagation, *Geophys. Prospect.,* **34,** 686–703.

Bradford, J.H., Clement, W.P. & Barrash, W., 2009. Estimating porosity with ground-penetrating radar reflection tomography: a controlled 3-D experiment at the Boise Hydrogeophysical Research Site, *Water Resour. Res.,* **45,** doi:10.1029/2008wr006960.

Busch, S., van der Kruk, J., Bikowski, J. & Vereecken, H., 2012. Quantitative conductivity and permittivity estimation using full-waveform inversion of on-ground GPR data, *Geophysics,* **77,** H79–H91.

Buursink, M.L., Johnson, T.C., Routh, P.S. & Knoll, M.D., 2008. Crosshole radar velocity tomography with finite-frequency Fresnel volume sensitivities, *Geophys. J. Int.,* **172,** 1–17.

Cirpka, O.A., Fienen, M.N., Hofer, M., Hoehn, E., Tessarini, A., Kipfer, R. & Kitanidis, P.K., 2007. Analyzing bank filtration by deconvoluting time series of electric conductivity, *Ground Water,* **45,** 318–328.

Cordua, K.S., Hansen, T.M. & Mosegaard, K., 2012. Monte Carlo full-waveform inversion of crosshole GPR data using multiple-point geostatistical a priori information, *Geophysics,* **77,** H19–H31.

Coscia, I., Greenhalgh, S.A., Linde, N., Doetsch, J., Marescot, L., Gunther, T., Vogt, T. & Green, A.G., 2011. 3D crosshole ERT for aquifer characterization and monitoring of infiltrating river water, *Geophysics,* **76,** G49–G59.

Coscia, I., Linde, N., Greenhalgh, S., Vogt, T. & Green, A., 2012. Estimating traveltimes and groundwater flow patterns using 3D time-lapse crosshole ERT imaging of electrical resistivity fluctuations induced by infiltrating river water, *Geophysics,* **77,** E239–E250.

Dafflon, B., Irving, J. & Barrash, W., 2011. Inversion of multiple intersecting high-resolution crosshole GPR profiles for hydrological characterization at the Boise Hydrogeophysical Research Site, *J. appl. Geophys.,* **73,** 305–314.

Davis, J.L. & Annan, A.P., 1989. Ground-penetrating radar for high-resolution mapping of soil and rock stratigraphy, *Geophys. Prospect.,* **37,** 531–551.

Day-Lewis, F.D., Lane, J.W., Harris, J.M. & Gorelick, S.M., 2003. Time-lapse imaging of saline-tracer transport in fractured rock using difference-attenuation radar tomography, *Water Resour. Res.,* **39,** doi:10.1029/2002wr001722.

Day-Lewis, F.D., Singha, K. & Binley, A.M., 2005. Applying petrophysical models to radar travel time and electrical resistivity tomograms: resolution-dependent limitations, *J. geophys. Res.-Sol. Earth,* **110,** doi:10.1029/2004jb003569.

Diem, S., Vogt, T. & Hoehn, E., 2010. Spatial characterization of hydraulic conductivity in alluvial gravel-and-sand aquifers: a comparison of methods, *Grundwasser,* **15,** 241–251.

Doetsch, J., Linde, N., Coscia, I., Greenhalgh, S.A. & Green, A.G., 2010a. Zonation for 3D aquifer characterization based on joint inversions of multimethod crosshole geophysical data, *Geophysics,* **75,** G53–G64.

Doetsch, J.A., Coscia, I., Greenhalgh, S., Linde, N., Green, A. & Gunther, T., 2010b. The borehole-fluid effect in electrical resistivity imaging, *Geophysics,* **75,** F107–F114.

Dogan, M., Van Dam, R.L., Bohling, G.C., Butler, J.J. & Hyndman, D.W., 2011. Hydrostratigraphic analysis of the MADE site with full-resolution GPR and direct-push hydraulic profiling, *Geophys. Res. Lett.,* **38,** doi:10.1029/2010GL046439.

Dorn, C., Linde, N., Doetsch, J., Le Borgne, T. & Bour, O., 2012. Fracture imaging within a granitic rock aquifer using multiple-offset single-hole and cross-hole GPR reflection data, *J. appl. Geophys.,* **78,** 123–132.

Ernst, J.R., Green, A.G., Maurer, H. & Holliger, K., 2007a. Application of a new 2D time-domain full-waveform inversion scheme to crosshole radar data, *Geophysics,* **72,** J53–J64.

Ernst, J.R., Maurer, H., Green, A.G. & Holliger, K., 2007b. Full-waveform inversion of crosshole radar data based on 2-D finite-difference time-domain solutions of Maxwell's equations, *IEEE Trans. Geosci. Remote Sens.,* **45,** 2807–2828.

Fichtner, A. & Trampert, J., 2011. Resolution analysis in full waveform inversion, *Geophys. J. Int.,* **187,** 1604–1624.

Garambois, S., Senechal, P. & Perroud, H., 2002. On the use of combined geophysical methods to assess water content and water conductivity of near-surface formations, *J. Hydrol.,* **259,** 32–48.

Hubbard, S.S. & Rubin, Y., 2000. Hydrogeological parameter estimation using geophysical data: a review of selected techniques, *J. Contam. Hydrol.,* **45,** 3–34.

Hubbard, S.S., Rubin, Y. & Majer, E., 1997. Ground-penetrating-radar-assisted saturation and permeability estimation in bimodal systems, *Water Resour. Res.,* **33,** 971–990.

Hubbard, S.S., Chen, J.S., Peterson, J., Majer, E.L., Williams, K.H., Swift, D.J., Mailloux, B. & Rubin, Y., 2001. Hydrogeological characterization of the South Oyster Bacterial Transport Site using geophysical data, *Water Resour. Res.,* **37,** 2431–2456.

Kemna, A., Vanderborght, J., Kulessa, B. & Vereecken, H., 2002. Imaging and characterisation of subsurface solute transport using electrical resistivity tomography (ERT) and equivalent transport models, *J. Hydrol.,* **267,** 125–146.

Klotzsche, A., van der Kruk, J., Meles, G.A., Doetsch, J., Maurer, H. & Linde, N., 2010. Full-waveform inversion of cross-hole ground-penetrating radar data to characterize a gravel aquifer close to the Thur River, Switzerland, *Near. Surf. Geophys.,* **8,** 635–649.

Klotzsche, A., van der Kruk, J., Meles, G.A. & Vereecken, H., 2012. Cross-hole GPR full-waveform inversion of waveguides acting as preferential flow paths within aquifer systems, *Geophysics,* **77,** H57–H62.

Kuroda, S., Takeuchi, M. & Kim, H.J., 2007. Full-waveform inversion algorithm for interpreting crosshole radar data: a theoretical approach, *Geosci. J.,* **11,** 211–217.

Linde, N., Binley, A., Tryggvason, A., Pedersen, L.B. & Revil, A., 2006. Improved hydrogeophysical characterization using joint inversion of cross-hole electrical resistance and ground-penetrating radar traveltime data, *Water Resour. Res.,* **42,** doi:10.1029/2006WR005131.

Lochbühler, T., Doetsch, J., Brauchler, R. & Linde, N., 2013. Structure-coupled joint inversion of geophysical and hydrological data, *Geophysics,* **78,** ID1–ID14.

Looms, M.C., Jensen, K.H., Binley, A. & Nielsen, L., 2008. Monitoring unsaturated flow and transport using cross-borehole geophysical methods, *Vadose Zone J.,* **7,** 227–237.

Meles, G., Van der Kruk, J., Greenhalgh, S.A., Ernst, J.R., Maurer, H. & Green, A.G., 2010. A new vector waveform inversion algorithm for simultaneous updating of conductivity and permittivity parameters from combination crosshole/borehole-to-surface GPR data, *IEEE Trans. Geosci. Remote Sens.,* **48,** 3391–3407.

Meles, G., Greenhalgh, S., van der Kruk, J., Green, A. & Maurer, H., 2011. Taming the non-linearity problem in GPR full-waveform inversion for high contrast media, *J. appl. Geophys.,* **73,** 174–186.

Musil, M., Maurer, H., Hollinger, K. & Green, A.G., 2006. Internal structure of an alpine rock glacier based on crosshole georadar traveltimes and amplitudes, *Geophys. Prospect.,* **54,** 273–285.

Oberröhrmann, M., Klotzsche, A., van der Kruk, J. & Vereecken, H., 2013. Optimization of acquisition setup for cross-hole GPR full waveform inversion using checkerboard analysis, *Near Surf. Geophys.,* **11,** 197–209.

Pratt, R.G. & Shipp, R.M., 1999. Seismic waveform inversion in the frequency domain, part 2: fault delineation in sediments using crosshole data, *Geophysics,* **64,** 902–914.

Pride, S., 1994. Govering equations for the coupled electromagnetics and acoustics of porous-media, *Physical Rev.,* **50,** 15 678–15 696.

Rao, Y., Wang, Y.H. & Morgan, J.V., 2006. Crosshole seismic waveform tomography: II. Resolution analysis, *Geophys. J. Int.,* **166,** 1237–1248.

Ronayne, M.J. & Gorelick, S.M., 2006. Effective permeability of porous media containing branching channel networks, *Phys. Rev. E,* **73,** doi:10.1103/PhysRevE.73.026305.

Rubin, Y., Mavko, G. & Harris, J., 1992. Mapping permeability in heterogeneous aquifers using hydrologic and seismic data, *Water Resour. Res.,* **28,** 1809–1816.

Shin, C. & Cha, Y.H., 2008. Waveform inversion in the Laplace domain, *Geophys. J. Int.,* **173,** 922–931.

Slater, L.D. *et al.*, 2010. Use of electrical imaging and distributed temperature sensing methods to characterize surface water-groundwater exchange regulating uranium transport at the Hanford 300 Area, Washington, *Water Resour. Res.,* **46,** doi:10.1029/2010wr009110.

Streich, R. & van der Kruk, J., 2007. Characterizing a GPR antenna system by near-field electric field measurements, *Geophysics,* **72,** A51–A55.

Strobach, E., Harris, B.D., Dupuis, J.C., Kepic, A.W. & Martin, M.W., 2012. Cross well radar and vertical radar profiling methods for time lapse monitoring of rainfall infiltration, in *ASEG Extended Abstracts,* pp. 1–4.

Strobach, E., Harris, B.D., Dupuis, J.C. & Kepic, A.W., 2013. Waveguide properties recovered from shallow diffractions in common offset GPR, *J. geophys. Res.-Sol. Earth,* **118,** 1–12.

Tarantola, A., 1984. Inversion of seismic-reflection data in the acoustic approximation, *Geophysics,* **49,** 1259–1266.

Tarantola, A., 2005. *Inverse Problem Theory and Methods for Model Parameter Estimation,* Society for Industrial and Applied Mathematics, Philadelphia, PA.

Tchang, T., 2012. Intégration de donnés géophysiques pour obtenir un modèle en trois dimensions d'un aquifère au voisinage de la rivière Thur, Suisse, *MSc thesis,* University of Lausanne, Lausanne.

Tronicke, J., Blindow, N., Gross, R. & Lange, M.A., 1999. Joint application of surface electrical resistivity and GPR-measurements for groundwater exploration on the island of Spiekeroog—northern Germany, *J. Hydrol.,* **223,** 44–53.

Tronicke, J., Dietrich, P., Wahlig, U. & Appel, E., 2002. Integrating surface georadar and crosshole radar tomography: a validation experiment in braided stream deposits, *Geophysics,* **67,** 1516–1523.

Tronicke, J., Holliger, K., Barrash, W. & Knoll, M.D., 2004. Multivariate analysis of cross-hole georadar velocity and attenuation tomograms for aquifer zonation, *Water Resour. Res.,* **40,** W01519, doi:10.1029/2003WR002031.

van der Kruk, J., Steelman, C.M., Endres, A.L. & Vereecken, H., 2009. Dispersion inversion of electromagnetic pulse propagation within freezing and thawing soil waveguides, *Geophys. Res. Lett.,* **36,** L18503, doi:10.1029/2009GL039581.

van der Kruk, J., Jacob, R.W. & Vereecken, H., 2010. Properties of precipitation-induced multilayer surface waveguides derived from inversion of dispersive TE and TM GPR data, *Geophysics,* **75,** Wa263–Wa273.

Virieux, J. & Operto, S., 2009. An overview of full-waveform inversion in exploration geophysics, *Geophysics,* **74,** WCC1–WCC26.

Williamson, P.R., 1991. A guide to the limits of resolution imposed by scattering in ray tomography, *Geophysics,* **56,** 202–207.

Winship, P., Binley, A. & Gomez, D., 2006. Flow and transport in the unsaturated Sherwood Sandstone: characterization using cross-borehole geophysical methods, in *Fluid Flow and Solute Movement in Sandstones: the Onshore UK Permo-Triassic Red Bed Sequence,* pp. 219–231, eds Barker, R.D. & Tellam, J.H. Geological Society, London.

Wu, R.S. & Toksoz, M.N., 1987. Diffraction tomography and multisource holography applied to seismic imaging, *Geophysics,* **52,** 11–25.

Zhang, F.J., Juhlin, C., Cosma, C., Tryggvason, A. & Pratt, R.G., 2012. Cross-well seismic waveform tomography for monitoring CO2 injection: a case study from the Ketzin Site, Germany, *Geophys. J. Int.,* **189,** 629–646.

Zheng, C.M., Bianchi, M. & Gorelick, S.M., 2011. Lessons learned from 25 years of research at the MADE site, *Ground Water,* **49,** 649–662.